Available online at www.sciencedirect.com

ScienceDirect

Proceedings of the Combustion Institute 38 (2021) 6203–6211

Proceedings of the Combustion Institute

www.elsevier.com/locate/proci

Analysis of core-noise contributions in a realistic gas-turbine combustor operated near lean blow-out

Changxiao Shao, Kazuki Maeda, Matthias Ihme*

Department of Mechanical Engineering, Stanford University, Stanford, CA 94305, USA

Received 8 November 2019; accepted 19 July 2020
Available online 19 November 2020

Abstract

The relative importance of direct and indirect combustion noise in a realistic gas-turbine combustor is investigated. While temperature fluctuations are commonly recognized as the primary source of indirect combustion noise, recent theoretical analysis has shown that mixture inhomogeneities and associated variations in the Gibbs free energy represent another indirect noise-source contribution that is further investigated in this study. To this end, a hybrid model is developed that combines large-eddy simulations for predicting the unsteady turbulent reacting flow field in the combustor with a linearized Euler solver to describe the transmission and generation of noise through the downstream nozzle. By considering an operating point near the lean blow-out limit at cruise conditions, it is shown that indirect noise has an appreciable contribution to the overall noise emission at low frequencies, and direct noise arising from a tonal instability in the combustor dominates at higher frequencies. At this operating point, indirect noise contributing from compositional inhomogeneities was found to be comparable in magnitude to entropy noise from temperature inhomogeneities. A modal analysis of the indirect noise sources showed that the entropy and compositional noise are shifted in phase, resulting in a cancellation of the indirect noise. Effects of Mach number and modal shape of the combustor-exit perturbations on the noise generation are investigated, demonstrating the importance of spatial inhomogeneities to the core-noise contribution.

Keywords: Combustion noise; Indirect noise; Gas-turbine combustor; Large-eddy simulations

1. Introduction

The understanding, prediction, and mitigation of engine noise has received significant attention due to increasingly stringent requirements on noise reduction and anticipated growth in air traffic. Engine noise can be distinguished into fan noise, jet noise and core noise [1]. With recent progress towards the reduction of fan noise and jet noise, the relative contribution of core noise has increased in importance. Furthermore, with increasing interest in employing lean-premixed combustion technologies and the consideration of compact combustors that operate at higher pressures and power densi-

* Corresponding author.
E-mail address: mihme@stanford.edu (M. Ihme).

https://doi.org/10.1016/j.proci.2020.07.078
1540-7489

ties [2], it is anticipated that combustion-generated noise will further increase in importance.

Different mechanisms that contribute to core noise have been identified [3–6]. The first one is direct combustion noise, which describes the transmission of pressure fluctuations originating from the unsteady heat release in the combustion chamber [3]. The second one is indirect combustion noise that is caused by the convection of unsteady vortices, and entropy variations by temperature hot spots as they propagate from the combustor to the downstream turbine and nozzle [7]. More recently, contributions from mixture inhomogeneities and associated variations in the Gibbs free energy were identified as an additional source of indirect combustion noise that has so far not been considered [6,8]. The relative contribution of these noise-source mechanisms is strongly dependent on the operating conditions, engine type, and the interaction with other noise source.

Experiments have been conducted to examine combustion noise. With relevance to the analysis of indirect noise, Bake et al. [9] conducted measurements in an entropy wave generator to examine entropy noise mechanisms by heating. More recently, Rolland et al. [10] performed measurements in a similar configuration to quantify contributions from direct noise, entropy noise, and compositional noise, showing that experimental measurements for indirect noise are in good agreement with theoretical models.

Over recent years, significant progress has been made on the theoretical analysis of core noise. Acoustic analogies have been employed to characterize direct noise and jet-exhaust noise, and different methods have been proposed for modeling indirect noise that include the compact nozzle theory [7,11], the effective nozzle length method [12,13], expansion methods [14,15], and non-linear analysis [16].

With increasing computational resources, multidimensional simulations have been employed to investigate core noise [6]. Leyko et al. [17] compared direct and indirect noise mechanisms in a model combustor and found that indirect noise is small for laboratory experiments but increases for more realistic aeronautical engines. By using large-eddy simulation (LES), Papadogiannis et al. [18] assessed the generation of entropy noise in a high-pressure turbine stage and found that the upstream entropy noise is reduced due to the choked turbine nozzle guide vane. O'Brien et al. [19] employed a hybrid modeling approach to predict the core noise in a configuration that consists of combustor, turbine, nozzle and far-field radiation. Livebardon et al. [20] combined LES and actuator disk theory to predict combustion noise in a helicopter engine, confirming the importance of indirect combustion noise.

These experimental and computational investigations have shown that the relative contribution of direct and indirect noise to the overall core-noise radiation depends on engine type and operating conditions, and an integrated engine-flow-path representation requires consideration for predicting the noise transmission. By addressing this need, the objective of this study is to develop a hybrid model and investigate the relative importance of core-noise sources in a realistic gas-turbine combustor. The experimental configuration is presented in Section 2. The hybrid modeling approach is presented in Section 3. Results are analyzed in Section 4 and conclusions are provided in Section 5.

2. Experimental configuration

The combustor considered in this study was designed to reproduce features of a realistic rich-quench-lean (RQL) combustion chamber [21–23]. The air flow to the primary combustion zone is supplied through two outer axial swirlers and an inner radial swirler. The liquid fuel is injected through a pressure-swirl atomizer nested in the center. The combustor walls consist of multi-perforated liners and dilution holes. The total air flow mass rate is 391.4 g/s with temperature of 394 K. The fuel with temperature of 322 K is injected at an overall equivalence ratio of 0.1. The operating condition is representative for cruise conditions with an operating point near the lean blow-out limit [22]. The liquid fuel, considered in this study, consists of an alternative fuel with a low Derived Cetane Number (Cat-C1, POSF11498), and relevant fuel properties are summarized in Table 1. The pressure in the combustion chamber is 2.07 atm. Further details on

Table 1
Properties of the Cat-C1 fuel, with W: Molecular weight, Δh_C: Heat of combustion, H/C: Hydrogen/carbon ratio; μ_l: Dynamic viscosity of the liquid fuel, and DCN: Derived cetane number.

Composition (mass fraction [%])				
Aromatics	iso-Paraffins	n-Paraffins	Cycloparaffins	Alkenes
<0.01	99.63	<0.001	0.05	0.32
W [kg/kmol]	Δh_C [MJ/kg]	H/C	μ_l (322 K) [mPa s]	DCN
178	43.8	2.16	0.98	17.1

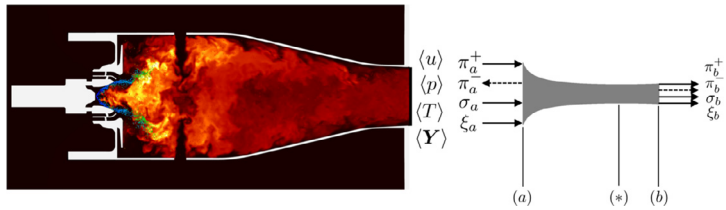

Fig. 1. Schematic of hybrid model that consists of unsteady combustor LES and low-order nozzle simulation.

physical properties and combustion quantities for droplet evaporation, flame-speed and ignition delay are provided as Supplementary Material.

3. Numerical method

3.1. Hybrid method

A hybrid model is developed to predict the combustion noise in a realistic combustor-nozzle configuration, which is illustrated in Fig. 1. In this hybrid model, an unsteady 3D combustion LES is employed to predict the turbulent reacting flow field in order to provide realistic combustor exit conditions as inflow to the downstream nozzle. The nozzle flow is described as solution to the linearized Euler equations (LEE), and inlet conditions for velocity, pressure, entropy, and mixture fraction are extracted from the upstream combustor simulation. In the absence of a detailed description of the downstream flow geometry, we considered a nozzle that expands the flow into the ambient at a prescribed nozzle-exit Mach-number M_b. The nozzle geometry is represented by a converging-diverging supersonic nozzle and the flow in the nozzle follows the linear-velocity profile by Duran and Moreau [14]. To examine effects of modal structure, spectral content, and noise-source contributions of the combustor-exit flow-field, we considered an idealized nozzle geometry. Further extensions are necessary to examine effects of the inlet-guide vanes, rotating blade-geometry, and blade cooling that are currently not considered with this idealized configuration.

3.2. Combustor simulations

Numerical simulations of the 3D combustor configuration are performed using a compressible LES-solver [24,25]. In this method the Favre-filtered conservation equations for mass, momentum and total specific energy are solved, and the thermochemical state is obtained from a flamelet/progress variable combustion model [26,27]. Further details on the computational model and LES-formulation are provided as Supplementary Material.

The governing equations are discretized using a hybrid scheme that combines a 4th-order accurate central schemes with a 2nd-order ENO scheme. Operator splitting is employed for time integration, in which the non-stiff advection-diffusion operators are solved using a third-order accurate strong-stability preserving Runge–Kutta scheme [28]. To integrate the stiff chemical source terms, a semi-implicit Rosenbrock–Krylov scheme is used, having 4^{th}-order accuracy and linear cost with respect to the number of species [29].

A Lagrangian spray particle model is employed to describe the disperse phase, which is two-way-coupled to the Eulerian gas-phase solver. The liquid fuel is injected following a Rosin–Rammler distribution and secondary atomization is modeled using a stochastic breakup model. The Vreman SGS model [30] is employed to model the turbulent stresses and the turbulence/chemistry interaction is represented using a presumed probability density function. Boundary conditions are prescribed by no-slip wall conditions and the effusive cooling is modeled through a homogeneous approach, in which the effusive gas-phase velocity is determined from measurements [22].

The combustor geometry is discretized using a hexahedral mesh with 18.3 million elements. The mesh is locally refined in the combustion and shear-layer regions. Studies on the mesh sensitivity were performed in prior work [22], focusing on predicting flame-shape, disperse phase, and capturing the blow-out limits, ensure that this simulation setup is adequate to describe the unsteady combustion process. Combustion noise is dominant at low frequencies [6], and the dissipation/dispersion properties of the LES solver were evaluated to ensure that the direct noise is accurately predicted for frequencies below 1.5 kHz.

A constant timestep of 50 ns is used to advance the solution in time. After the simulation reaches a steady state, statistics are collected for 35 ms, corresponding to seven characteristic residence times, $\tau_{res} = 5$ ms. By analyzing the flow field, we identified that the combustor exhibits a characteristic longitudinal frequency at $f_c = 400$ Hz. Probe measurements were employed to compute the acoustic spectra and longitudinal mode. In the experiment, Monfort et al. [21] observed an acoustic instability between 350 and 450 Hz for the equivalence ratio of 0.1, which agrees well with our simulation results.

3.3. Coupling of combustor exit and nozzle flow

The combustor exit with a rectangular shape is connected to the nozzle inlet (75 mm in width). To describe the nozzle flow, a Cartesian coordinate system is introduced in which the combustor exit lies on the $y-z$ plane and the x-axis is aligned with the nozzle center line. The combustor exit-flow was well mixed along the spanwise direction, allowing us to represent the nozzle-inlet flow as two-dimensional by averaging along the spanwise direction z. To describe the nozzle inlet conditions, we decompose the instantaneous filtered flow field $q = \{\widetilde{\boldsymbol{u}}, \overline{p}, \widetilde{s}, \widetilde{Z}\}$ (with $\boldsymbol{u}$: velocity vector, p: pressure, s: entropy, and Z: mixture fraction) at the combustor exit plane into mean and fluctuating quantities as $q(y,t) = \overline{q}(y) + q'(y,t)$. We further express the fluctuation in terms of temporal frequency as $q'(y,t) = \int A_q(y,f)\exp\{-i(2\pi ft + \phi_q)\}df$, where A_q, f, and ϕ_q are the amplitude, temporal frequency, and phase, respectively.

In the following, we adopt two methods to specify the amplitude, A_q. The first method assumes that q is uniform along the y-direction, allowing us to describe the perturbation by a planar mode shape. We spatially average each flow variable as $\langle q'\rangle_y(t) = H^{-1}\int q'(y,t)dy$, where H is the height of the combustor exit. A Fourier transformation of $\langle q'\rangle_y$ is performed to obtain the spatially averaged amplitude spectrum, $\langle A_q\rangle_y(f) = \mathcal{F}[\langle q'\rangle_y(t)]$. We conduct LEE simulations for various Mach numbers and various frequencies using this method.

The second method considers the component of fluctuations at the characteristic frequency $f = f_c$. To this end, we first apply a band-pass filter to the LES data to extract the corresponding frequency component of the flow variable at the combustor's exit plane. Proper orthogonal decomposition (POD) is then applied to the filtered data, and the first most-energetic spatial POD mode is applied to prescribe the spatial dependence of A_q. POD is a modal decomposition that extracts coherent spatial structures from dynamic data. Using a dominant POD mode as a boundary condition to the LEE simulation provides an adequate representation of the disturbance energy at the combustor exit as an effective noise source [31]. Note that, in the present analysis, POD is separately conducted to p', $\boldsymbol{u}'$, s', and Z' to extract the 1st POD mode of each of the variables. The effect of the mode shape on the combustion noise is discussed by comparing with results obtained using planar and Gaussian spatial distributions.

3.4. Nozzle-flow simulations

The flow through the nozzle is described from the solution of the linearized Euler equations that are obtained by decomposing the flow variables for a multicomponent mixture with frozen chemistry into a mean flow and fluctuations. Substituting the decomposed variables and retaining only first-order terms, the linearized Euler equations can then be written as:

$$\overline{D}_t s' + \boldsymbol{u}'\cdot\nabla\bar{s} = 0, \tag{1a}$$

$$\overline{D}_t\boldsymbol{u}' + \boldsymbol{u}'\cdot\nabla\boldsymbol{u} + \nabla p'/\bar{\rho} + \left(p'/\gamma\bar{p} - s'/c_p - \Psi Z'\right)\overline{\boldsymbol{u}}\cdot\nabla\overline{\boldsymbol{u}} = 0\,, \tag{1b}$$

$$\overline{D}_t p' + \boldsymbol{u}'\cdot\nabla\bar{p} + \gamma\left(\bar{p}\nabla\cdot\boldsymbol{u}' + p'\nabla\cdot\overline{\boldsymbol{u}}\right) = 0\,, \tag{1c}$$

$$\overline{D}_t Z' + \boldsymbol{u}'\cdot\nabla\bar{Z} = 0\,, \tag{1d}$$

where ρ is the density, c_p is the heat capacities, γ is the ratio of heat capacities, and Ψ is the chemical potential function. The governing equations are solved using a 4th-order finite difference scheme in conjunction with a 4th-order Runge–Kutta method with a constant time-step size.

In the following, the transmission is predicted in the form of a transfer function that compares the magnitude of an imposed disturbance at the nozzle inlet to the resulting disturbance at the nozzle outlet. In these studies, the transfer function is conveniently expressed in characteristic form for the downstream and upstream acoustic waves, advected entropy perturbations, and compositional perturbations, $\pi^{\pm} = (p'/\gamma\bar{p} \pm u'/\bar{c})/2$, $\sigma = s'/c_p$, $\xi = Z'$. We also introduce the Helmholtz number as $He = fL/c$, where f is the perturbation frequency, L is the nozzle length and c is the speed of sound at the nozzle inlet.

In this context, it is noted that this hybrid model is one-way coupled and effects of the nozzle reflection to the combustor flow-field are not considered. We have computed the transfer function of the reflected wave, π_a^-, with respect to incoming perturbations by acoustic, entropy and compositional disturbances at the characteristic frequency $f_c = 400$ Hz, giving the following results: $\pi_a^-/\pi_a^+ = 0.41$, $\pi_a^-/\sigma_a = 0.02$ and $\pi_a^-/\xi_a = 0.08$. This suggests that the reflection by entropy and compositional perturbations are small, and a two-way coupled model is required to examining the importance of the acoustic nozzle reflection on the combustion dynamics.

4. Results and discussion

4.1. Combustor results

Instantaneous and statistical results showing axial velocity, temperature, mixture fraction, and OH* are presented in Fig. 2. It can be seen that a strong inner recirculation zone is formed near the swirler, and a smaller recirculation region in the secondary combustion zone behind the dilution holes. The high temperature region is visible in the primary combustion zone, and the flame is anchored in the injector region as shown by the OH* field in Fig. 2. Comparison of OH*-profiles with

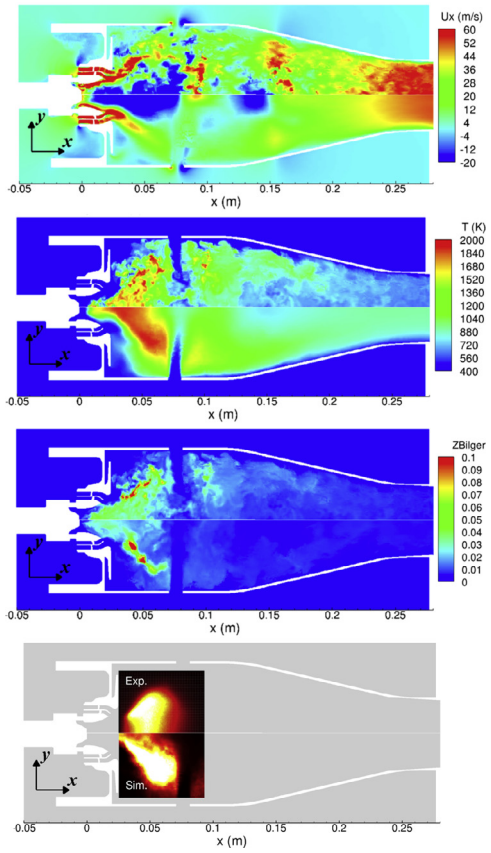

Fig. 2. Instantaneous and statistical results for axial velocity, temperature, mixture fraction, and OH* (from top to bottom), where the upper sub-panels show the instantaneous quantity and the lower sub-panels the time-averaged quantity; OH*-results are line-of-sight averaged data from experiments (top) and simulations (bottom).

measurements show reasonable agreement. Flow acceleration at the combustor exit can be seen and appreciable levels of inhomogeneities in the mixture composition and temperature field in the secondary combustion zone and at the combustor exit are visible.

Quantitative comparisons of droplet velocity with PDPA measurements are shown in Fig. 3 at three axial positions in the combustor, indicating that the present simulation can adequately reproduce the spray cone angle and the velocity magnitude. Mean combustor-exit quantities obtained from averaging across the exit plane are reported as: $\overline{p} = 1.975$ bar, $\overline{u} = 79.92$ m/s, $\overline{s} = 7.403$ KJ/(kg K), and $\overline{Z} = 0.008$.

4.2. Chemical potential function

The generation of indirect combustion noise by compositional inhomogeneities introduces a dependence on the chemical potential function, Ψ, as shown in Eq. (1). In this work, the chemical potential function is calculated from the flamelet solution in terms of Gibbs' free energy as a function of mixture fraction [6]:

$$\Psi = \frac{1}{c_p T} \sum_i \left(\frac{\mu_i}{W_i} - \Delta h_i^0 \right) \frac{dY_i}{dZ} = \frac{1}{c_p T} \frac{\partial g}{\partial Z} , \qquad (2)$$

where Δh_i^0 is the formation enthalpy, W_i is the molecular weight, T is the temperature, Y_i is the mass fraction, g is the specific Gibbs energy of the mixture. Here, we compute Ψ from a flamelet at scalar dissipation rate of $\chi = 1$ s^{-1}, which resembles the combustor exit condition. The chemical potential as a function of mixture fraction and Mach number M is illustrated in Fig. 4, showing a strong variation of Ψ at fuel-lean conditions and a direct dependence on M_b due to the dependence on temperature and pressure through Eq. (2).

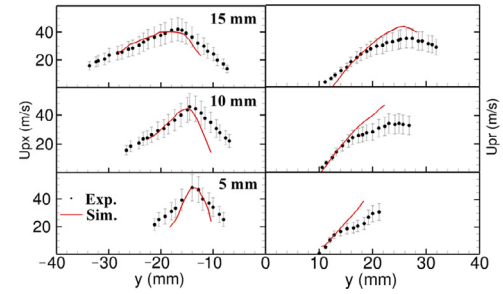

Fig. 3. Comparison of droplet velocity between experiment and simulation.

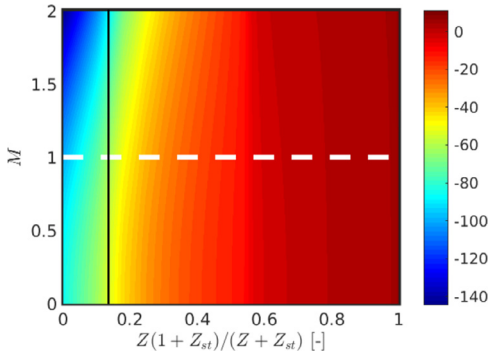

Fig. 4. Chemical potential Ψ as a function of rescaled mixture fraction and Mach number for Cat-C1 fuel.

4.3. Effect of Mach number

In this section, the relative importance of core-noise sources is investigated. For this, we consider nozzle-exit Mach numbers of $M_b = \{1.0, 1.25, 1.5\}$. The Helmholtz number is in the range of $0.2 < He < 2$, corresponding to physical

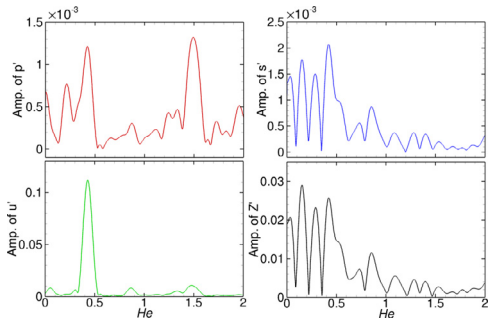

Fig. 5. Amplitude spectrum of pressure, axial velocity, entropy and mixture fraction fluctuations.

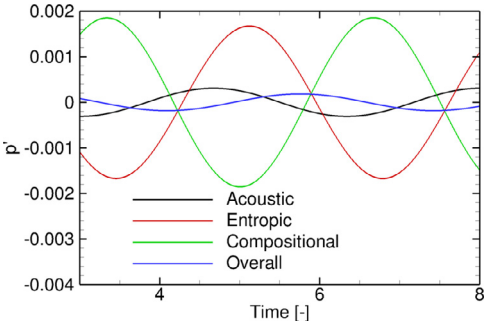

Fig. 7. Evolution of the acoustic, entropy, compositional, and total noise sampled at the center of the nozzle exit for the conditions $M_b = 1.5$ and $He = 0.2$.

frequencies of 200 Hz $< f <$ 2000 Hz with nozzle length $L = \{0.4, 0.45, 0.5\}$ m, respectively. Planar inlet perturbations are considered and the magnitude of the perturbation is obtained from the Fourier transformation of the combustor exit signal. Fig. 5 shows the amplitude spectrum of the combustor exit quantities.

We compare the sound pressure level (SPL) for different noise-source contributions for the three different nozzle-exit Mach numbers. The nozzle length is modified to match different outlet Mach numbers [14]. Results for the computed sound-pressure levels are shown in Fig. 6, where SPL is defined as $\mathrm{SPL} = 20\log_{10}(p_{\mathrm{rms}}/p'_0)$ dB, where p_{rms} p' is the root-mean-square of the sound pressure and p'_0 is the reference sound pressure of 20 μPa. It can be seen that the Mach number has a negligible effect on the SPL over the range of frequencies considered in this study. At $He = 0.2$, the entropy and compositional noise contributions dominate over the direct noise. This frequency is lower than the characteristic frequency of 400 Hz, which corresponds to $He = 0.4$. Over this frequency range, entropy and compositional noise are found to be more important for this operating condition. At $He = 0.4$, all noise sources reach their peak values. For conditions $He > 0.4$, the SPL for entropy and compositional noise decrease, while the direct noise attains an additional peak at $He = 1.5$. This frequency corresponds to the higher harmonic frequency, which is also observed in the spectrum of the pressure and velocity perturbations at the combustor exit, as shown in Fig. 5. Notably, for $He = 0.2$ and 1.0, the total noise is smaller than the compositional and entropy noise, which can be explained by the phase cancellation between both noise sources.

Fig. 7 shows the temporal evolution of the pressure perturbations at the center of the nozzle exit that correspond to the acoustic, entropy, compositional, and total noise contributions for the case with $M_b = 1.5$ at $He = 0.2$. We see that the entropy and compositional noise have similar amplitudes, but they are phase shifted by π. As a result, these two noise-sources cancel, so that their contribution to the total noise becomes small.

4.4. Effect of spatial mode shape

In previous theoretical investigations [7,8,11–15] and numerical simulations [32], perturbations at the nozzle inlet were treated as planar perturbations. However, the spatial distribution at the combustor exit may differ as a consequence of inhomogeneous combustor-exit flow field. In this section,

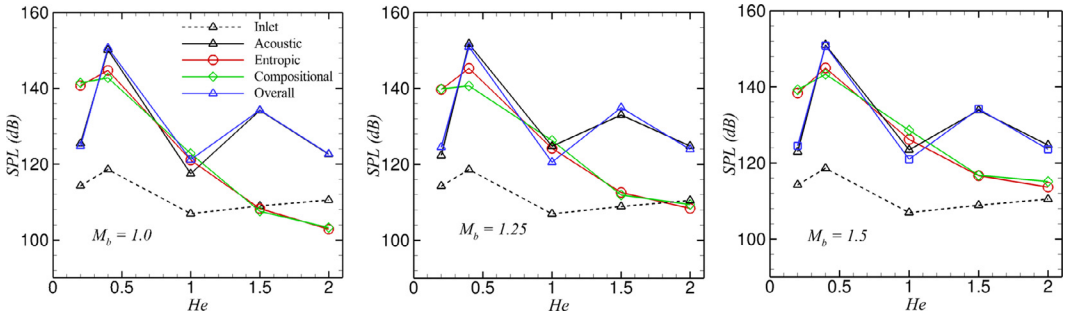

Fig. 6. Comparison of SPL for different noise sources and different outlet Mach numbers.

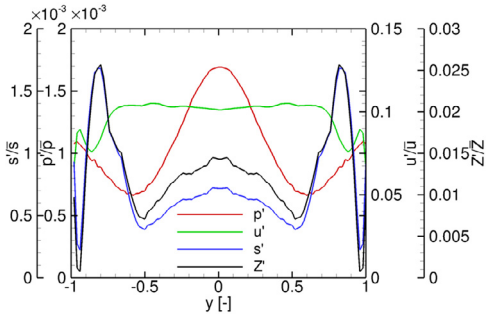

Fig. 8. First spatial POD modes $\psi_1(y)$ for pressure, velocity, entropy and mixture fraction fluctuations obtained from band-pass filtered LES data at the combustor exit. The amplitude is normalized.

we investigate effects of these spatial distributions on the resulting acoustic noise by directly considering the most energetic POD-modes that are computed from the LES data.

Fig. 8 shows the first POD mode shape for each quantity. We perform separate LEE simulations using these mode shapes as boundary conditions: $q'(y,t) = \psi_1(y)\sin(2\pi f_c t + \phi_q)$, where $\psi_1(y)$ is the most-energetic POD-mode and $\phi_q = 0$ for p', $-\pi/2$ for u', and $\pi/2$ for s' and Z', respectively. We also perform separate simulations with planar and Gaussian spatial distributions with the same total energy to that of the corresponding POD-mode.

Fig. 9 shows sets of instantaneous contours of the downstream-propagating acoustic waves in the nozzle obtained from the simulations using planar, Gaussian, and POD mode shapes with $He = 0.4$ and $M_b = 1.5$. Each set shows the acoustic waves that originate from the acoustic, entropy and compositional perturbations at the nozzle inlet. For all simulations, we observe strong spatial variations of the acoustic amplitude along the nozzle center. These variations correspond to the wavelength of the pressure perturbation. In contrast, vertical variations of the acoustic amplitude are strongly dependent on the boundary conditions at the inlet. This dependence is evident in the contours for the composition and entropy noise. With the Gaussian mode shape, the amplitude is larger at the nozzle center than at the nozzle wall. With the POD mode shape, a larger amplitude is observed near the nozzle wall. This spatial variation corresponds to the mode shapes at the inlet in that both the entropy and mixture fraction fluctuations take their maximum values at $y \approx \pm 1$ (Fig. 8).

Table 2
Comparison of SPL for different mode shapes.

	Planar (dB)	Gaussian (dB)	POD (dB)
Acoustic	152.34	162.58	160.24
Entropic	144.96	153.42	149.75
Compositional	143.29	152.91	150.39
Total	152.12	161.83	159.36

Table 2 compares SPL for acoustic, entropy, compositional, and total noise at the nozzle exit for the different inlet boundary conditions. For all noise contributions, the SPL is largest for the Gaus-

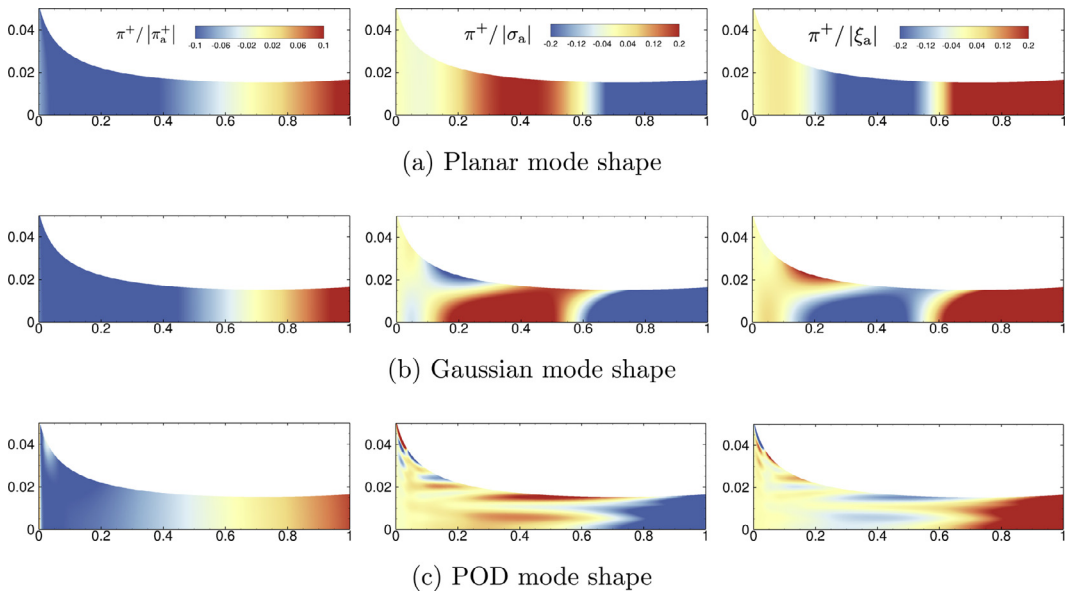

Fig. 9. Instantaneous contours of downstream-propagating acoustic waves for different spatial structure of acoustic, entropy and compositional perturbations at nozzle inlet for constant $He = 0.4$ and $M_b = 1.5$.

sian mode shape and smallest for the planar mode shape. Although the POD mode shapes at the inlet do not resemble the Gaussian mode structure (Fig. 8), their emitted acoustic energy is similar and differs only by few dBs. Overall, the results suggest that the spatial inhomogeneity of the inlet perturbations can significantly affect the SPL at the nozzle exit in a non-trivial manner. Therefore, the accurate consideration of the effect of these inhomogeneous combustor-exit conditions on the noise emission requires a coupled modeling approach.

5. Conclusions

In this study, the relative importance of direct and indirect combustion noise is examined by considering a hybrid modeling approach to couple a gas-turbine combustor with a converging-diverging nozzle. Effects of perturbation frequency, Mach number, and combustor exit modes on the noise generation are investigated. From this study, the following conclusions can be drawn:

- For the operating conditions examined, entropy and compositional noise sources have comparable contributions to the sound pressure level, with both exceeding the direct noise at low frequencies;
- The direct noise is found to be approximately 10 dB higher than the indirect noise at the characteristic combustor frequency of $He = 0.4$;
- The spatial mode shape has a significant effect on the acoustic transmission through the nozzle and requires consideration in accurately predicting the combustion noise.

In this study, we examined the generation and transmission of combustion noise in a representative RQL combustor and nozzle geometry. It is noted that this hybrid approach introduces limitation and further investigations are necessary to examine effects of turbomachinery, inlet guide vanes, and blade cooling.

Declaration of Competing Interest

The authors declare that they have no known competing financial interests or personal relationships that could have appeared to influence the work reported in this paper.

Acknowledgments

This research was supported by the AeroAcoustics Research Consortium with award number OAI-AARCS-19026 and NASA with award number NNX15AV04A. We thank Dr. Jeonglae Kim for sharing the LEE-solver, and Danyal Mohaddes and Dr. Quentin Douasbin are acknowledged for fruitful discussions on the acoustic analysis.

Supplementary material

Supplementary material associated with this article can be found, in the online version, at doi:10.1016/j.proci.2020.07.078

References

[1] J.R. Mahan, A. Karchmer, Combustion and core noise, in: H.H. Hubbard (Ed.), Aeroacoustics of Flight Vehicles, Theory and Practice–Volume 1: Noise Sources, Acoustics Society America, 1995, pp. 483–517.
[2] L.S. Hultgren, *Core Noise: Implications of Emerging N+3 Designs and Acoustic Technology Needs*, Acoustics Technical Working Group, 2011.
[3] W.C. Strahle, *Prog. Energy Combust. Sci.* 4 (1978) 157–176.
[4] S. Candel, D. Durox, S. Ducruix, A.-L. Birbaud, N. Noiray, T. Schuller, *Int. J. Aeroacoustics* 8 (1–2) (2009) 1–56.
[5] A.P. Dowling, Y. Mahmoudi, *Proc. Combust. Inst.* 35 (2015) 65–100.
[6] M. Ihme, *Ann. Rev. Fluid Mech.* 49 (2017) 277–310.
[7] F.E. Marble, S.M. Candel, *J. Sound Vib.* 55 (2) (1977) 225–243.
[8] L. Magri, J. O'Brien, M. Ihme, *J. Fluid Mech.* 799 (2016) R4.
[9] F. Bake, C. Richter, C. Mühlbauer, N. Kings, I. Röhle, F. Thiele, B. Noll, *J. Sound Vib.* 326 (2009) 574–598.
[10] E.O. Rolland, F. De Domenico, S. Hochgreb, *J. Eng. Gas Turb. Power* 140 (2018) 082604.
[11] N.A. Cumpsty, F.E. Marble, *J. Sound Vib.* 54 (2) (1977) 297–309.
[12] S.R. Stow, A.P. Dowling, T.P. Hynes, *J. Fluid Mech.* 467 (2002) 215–239.
[13] C.S. Goh, A.S. Morgans, *J. Sound Vib.* 330 (2011) 5184–5198.
[14] I. Duran, S. Moreau, *J. Fluid Mech.* 723 (2013) 190–231.
[15] I. Duran, A.S. Morgans, *J. Fluid Mech.* 773 (2015) 137–153.
[16] M. Huet, A. Giauque, *J. Fluid Mech.* 733 (2013) 268–301.
[17] M. Leyko, F. Nicoud, T. Poinsot, *AIAA J.* 47 (11) (2009) 2709–2716.
[18] D. Papadogiannis, G. Wang, S. Moreau, F. Duchaine, L. Gicquel, F. Nicoud, *J. Eng. Gas Turb. Power* 138 (041503) (2016) 1–8.
[19] J. O'Brien, J. Kim, M. Ihme, *AIAA Paper 2015–2821* (2015).
[20] T. Livebardon, S. Moreau, L. Gicquel, T. Poinsot, E. Bouty, *Combust. Flame* 165 (2016) 272–287.
[21] J.R. Monfort, S.D. Stouffer, T.H. Hendershott, P.J. Wrzesinski, W.S. Foley, K.D. Rein, *AIAA Paper 2017-1101* (2017).
[22] L. Esclapez, P.C. Ma, E. Mayhew, R. Xu, S. Stouffer, T. Lee, H. Wang, M. Ihme, *Combust. Flame* 181 (2017) 82–99.

[23] S. Stouffer, T. Hendershott, J.R. Monfort, J. Diemer, E. Corporan, P. Wrzesinski, A.W. Caswell, *AIAA Paper 2017-1954* (2017).
[24] Y. Khalighi, J.W. Nichols, S.K. Lele, F. Ham, P. Moin, *AIAA Paper 2011–2886* (2011).
[25] P.C. Ma, Y. Lv, M. Ihme, *J. Comput. Phys.* 340 (2017) 330–357.
[26] C.D. Pierce, P. Moin, *J. Fluid Mech.* 504 (2004) 73–97.
[27] M. Ihme, C.M. Cha, H. Pitsch, *Proc. Combust. Inst.* 30 (2005) 793–800.
[28] S. Gottlieb, C.W. Shu, E. Tadmor, *SIAM Rev.* 43 (1) (2001) 89–112.
[29] H. Wu, P.C. Ma, M. Ihme, *Comput. Phys. Commun.* 243 (2019) 81–96.
[30] A.W. Vreman, *Phys. Fluids* 16 (2004) 3670–3681.
[31] J.B. Freund, T. Colonius, *Int. J. Aeroacoust.* 8 (4) (2009) 337–354.
[32] L. Magri, J. OBrien, M. Ihme, *J. Eng. Gas Turbines Power* 140 (031501) (2018) 1–9.